Transurethral light delivery for prostate photoacoustic imaging

Muyinatu A. Lediju Bell
Xiaoyu Guo
Danny Y. Song
Emad M. Boctor

Transurethral light delivery for prostate photoacoustic imaging

Muyinatu A. Lediju Bell,[a,b,*] **Xiaoyu Guo,**[c] **Danny Y. Song,**[d] **and Emad M. Boctor**[a,b,c,*]
[a]Johns Hopkins University, CISST Engineering Research Center, Baltimore, Maryland 21218, United States
[b]Johns Hopkins University School of Medicine, Department of Radiology, Baltimore, Maryland 21205, United States
[c]Johns Hopkins University, Department of Electrical and Computer Engineering, Baltimore, Maryland 21218, United States
[d]Johns Hopkins University School of Medicine, Department of Radiation Oncology and Molecular Sciences, Baltimore, Maryland 21205, United States

Abstract. Photoacoustic imaging has broad clinical potential to enhance prostate cancer detection and treatment, yet it is challenged by the lack of minimally invasive, deeply penetrating light delivery methods that provide sufficient visualization of targets (e.g., tumors, contrast agents, brachytherapy seeds). We constructed a side-firing fiber prototype for transurethral photoacoustic imaging of prostates with a dual-array (linear and curvilinear) transrectal ultrasound probe. A method to calculate the surface area and, thereby, estimate the laser fluence at this fiber tip was derived, validated, applied to various design parameters, and used as an input to three-dimensional Monte Carlo simulations. Brachytherapy seeds implanted in phantom, *ex vivo*, and *in vivo* canine prostates at radial distances of 5 to 30 mm from the urethra were imaged with the fiber prototype transmitting 1064 nm wavelength light with 2 to 8 mJ pulse energy. Prebeamformed images were displayed in real time at a rate of 3 to 5 frames per second to guide fiber placement and beamformed offline. A conventional delay-and-sum beamformer provided decreasing seed contrast (23 to 9 dB) with increasing urethra-to-target distance, while the short-lag spatial coherence beamformer provided improved and relatively constant seed contrast (28 to 32 dB) regardless of distance, thus improving multitarget visualization in single and combined curvilinear images acquired with the fiber rotating and the probe fixed. The proposed light delivery and beamforming methods promise to improve key prostate cancer detection and treatment strategies. © The Authors. Published by SPIE under a Creative Commons Attribution 3.0 Unported License. Distribution or reproduction of this work in whole or in part requires full attribution of the original publication, including its DOI. [DOI: 10.1117/1.JBO.20.3.036002]

1 Introduction

Photoacoustic imaging has the potential to improve prostate cancer screening and treatment procedures,[1–3] particularly when visualization with conventional ultrasound (US) is poor due to factors such as suboptimal acoustic contrast between normal and malignant tissues, acoustic clutter, and shadow artifacts.[4–9] It is implemented by transmitting nanosecond laser pulses, which cause targets that have higher optical absorption than surrounding tissue (e.g., highly vascularized cancerous tumors[10] or metallic brachytherapy seeds[11,12]) to preferentially absorb the light, undergo thermoelastic expansion, and thereby generate pressure transients that are detected by a conventional US probe. Enhanced tumor visualization with photoacoustic imaging could potentially enable more targeted biopsies, thereby increasing specificity and reducing the 23 to 35% occurrence of false negatives.[13,14] Similarly, brachytherapy seed visualization with photoacoustic imaging[11,15–18] has the potential to reduce the 13 to 61% dose deviation errors caused by typical seed placement errors,[19,20] thereby mitigating the risks of urinary and rectal side effects.[21–23] Advanced photoacoustic imaging methods that

incorporate contrast agents,[24–26] frequency-domain analyses,[27] or coherence-based beamforming[28] offer promising access to additional molecular, structural, or quantitative tissue information for early-stage prostate cancer detection or more effective brachytherapy administration.

The broad clinical utility of photoacoustic imaging to improve prostate cancer detection, treatment, and assessment relies on a minimally invasive light delivery method that offers sufficient fluence to illuminate targets of interest within laser safety limits. Valluru et al.[29] proposed a transrectal light delivery method to achieve this goal. Although it is minimally invasive, as the optics could be integrated with current transrectal US probes, this approach is limited by poor light penetration through the rectal wall.[30,31] As an alternative, we previously proposed and demonstrated the feasibility of an interstitial, transperineal light delivery method to visualize prostate brachytherapy seeds in phantoms, *ex vivo* liver tissue, and *in vivo* prostates.[17,28] This option does not necessarily suffer from poor light penetration, as the light source may be positioned directly next to a target of interest, and it can be well integrated with brachytherapy and biopsy procedures, which already require direct access to prostatic tissue. Limitations of this interstitial photoacoustic imaging approach include artifacts caused by a photoacoustic effect at the fiber tip and additional acoustic interactions (e.g., echo clutter).[17]

---

*Address all correspondence to: Muyinatu A. Lediju Bell, E-mail: muyinatu.lediijubell@jhu.edu; Emad M. Boctor, Email: eboctor@jhmi.edu

Transurethral light delivery overcomes a majority of the stated limitations with transrectal and interstitial light delivery. Yaseen et al.[31] suggested transurethral light delivery for visualizing prostate cancer and demonstrated feasibility with a light source placed outside of a canine prostate. Our previous work demonstrated the feasibility of transurethral illumination for detecting brachytherapy seeds with a light source placed inside the urethra of *ex vivo* canine prostates and transrectal sound reception.[32] This transrectal approach was later determined to be optimal, compared to transurethral sound reception, according to a simulation study performed by El-Gohary et al.[33] In both approaches, the transurethral light source could be directed along the fiber axis (i.e., end-firing),[32] orthogonal to the fiber axis in one primary direction (i.e., side-firing),[32] or omnidirectionally orthogonal to the fiber axis (i.e., cylindrical irradiation).[34] There are additional design trade-offs among the choice of fiber diameter, ease of fiber insertion, laser safety, and light delivery through a urinary catheter, which is commonly utilized in brachytherapy procedures with typical outer diameters of 13 to 16 Fr (4.3 to 5.3 mm).

To the authors' knowledge, this paper is the first to provide practical evidence of transurethral photoacoustic imaging with a side-firing fiber and present associated design and safety considerations. We built a custom prototype based on our design and utilized it to visualize prostate brachytherapy seeds in phantom, *ex vivo*, and *in vivo* prostates. The main research objectives were to investigate the feasibility of the proposed design and to compare the resulting target detection with amplitude- and coherence-based beamformers based on quantitative assessments of contrast and comparative resolution. A method to calculate surface area is derived to determine if energy densities at the fiber tip comply with laser safety limits, and the derivation is utilized in three-dimensional (3-D) Monte Carlo simulations to quantify the relative fluence incident on seed-like targets.

2 Methods and Materials

2.1 Fiber Design and Prototype

The side-firing fiber was custom designed as shown in Fig. 1(a) and described in our previous publication.[32] A multimode 1-mm core diameter optical fiber (Thorlabs, Newton, New Jersey) with a numerical aperture (NA) of 0.39 was polished at a 45 deg angle. This angle directed a fraction of the light 90 deg to the fiber axis using principles of total internal reflection. To collect and reuse the remaining light directed at an angle <90 deg to the fiber axis, a mirror was constructed from a metal rod polished to a 45 deg angle. The fiber and mirror were inserted into opposite ends of a quartz tube and oriented with their polished faces coincident to each other. The tube had an outer diameter of 2 mm. Epoxy was used to permanently fix the fiber and mirror in this orientation inside the quartz tube and create the side-firing fiber prototype shown in Fig. 1(b). An external marker was placed to visually track the direction of the laser beam. Visible 635-nm light was coupled to the free end of the fiber to display the profile of light that exits the fiber. The area of the emitted light on the surface of the quartz tube was estimated by resting a white sheet of paper on the tube, directing light toward this sheet, and observing the projection of this light onto the sheet, as shown in Fig. 1(c).

2.2 Surface Area and Energy Density Calculations

The laser spot size on the surface of the quartz tube can be approximated as an ellipse with a long axis ℓ and short axis S, as illustrated in Fig. 2(a). The long and short axes were derived by considering the longitudinal and axial cross-sectional views shown in Figs. 2(b) and 2(c), respectively. Fundamental principles of geometrical optics, with assumptions that all light is redirected 90 deg to the fiber axis, the fiber and tube are concentric, and the air gap between them is negligible, yield the following equations:

$$\ell = 2(R + R_{\text{tube}} \tan \theta), \tag{1}$$

$$S = 2R_{\text{tube}}(\alpha + \gamma_e), \tag{2}$$

where R and R_{tube} are the outer radii of the fiber and quartz tube, respectively, θ is the half-angle of the light cone exiting the fiber in air (estimated from the NA and the index of refraction in air, n_{air}), α is the angle of refraction in the fiber (estimated from the NA and index of refraction in glass, n_{glass}), and γ_e is the difference between α and the half-angle of the light exiting the quartz tube in the cross-section of Fig. 2(c):

$$\gamma_e = \sin^{-1}\left(\frac{R}{R_{\text{tube}}} \frac{n_{\text{air}}}{n_{\text{glass}}}\right). \tag{3}$$

Given the similarity of Eq. (3) to the critical angle for total internal reflection in the fiber [i.e., $\gamma = \sin^{-1}(n_{\text{air}}/n_{\text{glass}})$],[35] γ_e can be thought of as the effective critical angle of the light after passing through the quartz tube. Inserting Eqs. (1) and (2) into the equation for the area of an ellipse yields the following equation:

(a) (b) (c)
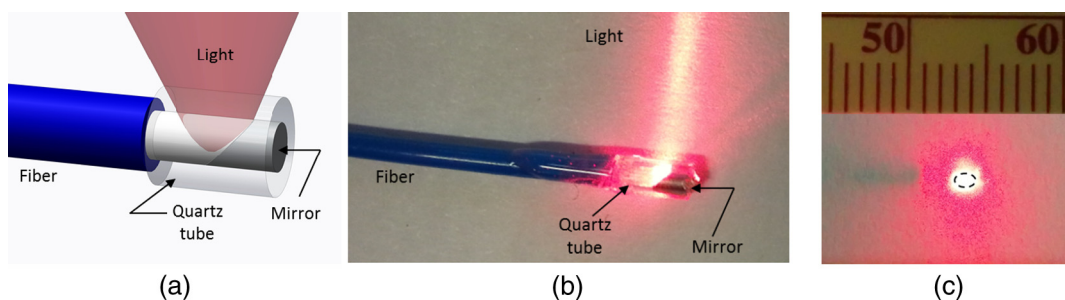
Fig. 1 (a) Design components of the side-firing fiber and photographs of (b) a custom-built fiber prototype and (c) the laser spot size projection on a sheet of paper resting on the surface of the quartz tube. The dashed ellipse was drawn to scale on the photograph to show the perimeter of the surface area calculated with Eq. (4) and the design parameters listed in Table 1. The scale has units of millimeter.
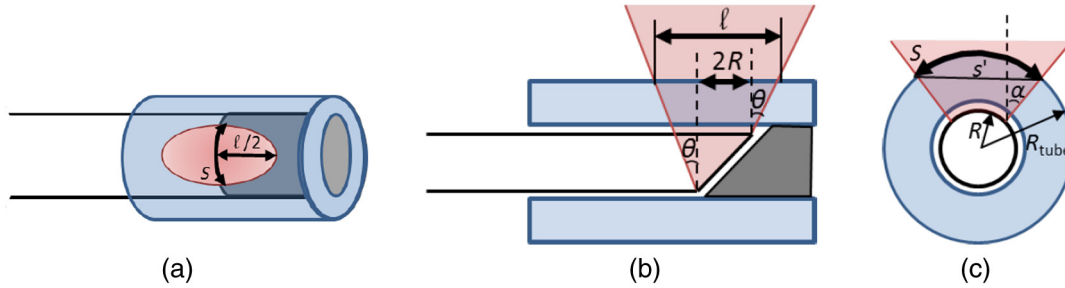
Fig. 2 (a) Schematic diagram showing the dimensions of the laser spot size on the surface of the quartz tube. Dimensions of the light emitted in (b) longitudinal and (c) axial cross-sections of the fiber are related to the fiber design parameters.

$$\text{Surface area} = \pi(\alpha + \gamma_e)(RR_{\text{tube}} + R_{\text{tube}}^2 \tan \theta). \qquad (4)$$

The design parameters for the side-firing fiber shown in Fig. 1 are reported in Table 1. Inserting these parameters into the above equations yields $\ell = 1.8$ mm, $S = 1.2$ mm, and Area = 1.7 mm^2, which are reasonable estimates, as indicated by the ellipse with these dimensions, superimposed on the laser spot photograph in Fig. 1(c). Equations (1)–(4) were used to estimate surface areas and corresponding energy densities for a range of NA values, fiber diameters, and tube diameters, and to determine the initial light profile for the simulations described in Sec. 2.4. In addition, the energy limit, E_{lim}, for a particular energy density limit, U_{lim}, was determined by combining the definition of energy density with Eq. (4) to achieve the following equation:

$$E_{\text{lim}} = U_{\text{lim}}\pi(\alpha + \gamma_e)(RR_{\text{tube}} + R_{\text{tube}}^2 \tan \theta). \qquad (5)$$

2.3 Phantom Experiments

The side-firing fiber prototype was coupled to a 1064-nm Q-switched Nd:YAG laser (Phocus InLine, Opotek, Carlsbad, California) with a 5 ns pulse duration and 10 Hz repetition rate. The resulting pulse energy was measured with and without the fiber inserted into a 16-Fr silicone urinary catheter (Model 1658-16 Bardex®, Bard Medical Division, Covington, Georgia). Energy losses due to the presence of the catheter were minimal.

A 4 cm × 2 cm × 10 cm plastisol phantom was drilled with a 4-mm-diameter hole to accommodate a 14-Fr urinary catheter and a 2-cm-diameter hole to insert the transrectal US probe. The relationship between the holes mimicked the relationship between the urethra and rectum. Decayed brachytherapy seeds (TheraSeed, Theragenics Corporation, Buford, Georgia) were inserted using a standard 18 G brachytherapy needle at radial distances of 0.5, 1, 2, and 3 cm from the center of the 4-mm hole, which corresponds to distances of 1.7, 2.3, 2.9, and 5.0 cm from the closest outer edge of the 2-cm hole, respectively. The seeds were cylindrical shells with an outer diameter of 0.8 mm and a long axis of 4.5 mm, coated with black India ink to increase optical absorption.[36] For clinical implementation, a biocompatible coating with similar optical absorption to India ink would be more suitable, which is a reasonable modification for seeds purposely designed for photoacoustic imaging considering that similar enhancement coatings are common in brachytherapy.[37]

After placing the catheter and probe in their respective holes, the side-firing fiber was inserted through the urinary catheter and rotated to visualize each seed individually, as illustrated in Fig. 3(a). A photograph of the actual phantom appears in Fig. 3(b), showing the holes for the probe and catheter as well as the implanted seeds. The average energy per pulse used to visualize the seeds was ∼2 mJ, which corresponds to

Table 1 Summary of side-firing fiber design parameters.

Parameter	Symbol	Value
Numerical aperture	NA	0.39
Index of refraction in air	n_{air}	1.00
Index of refraction in glass	n_{glass}	1.45
Half angle of light cone	θ	23.0 deg
Angle of refraction	α	15.6 deg
Critical angle	γ	43.6 deg
Effective critical angle	γ_e	20.2 deg
Radius of fiber core	R	0.5 mm
Radius of quartz tube	R_{tube}	1.0 mm
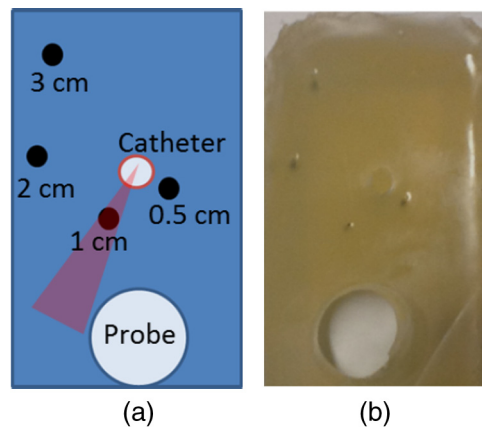
Fig. 3 (a) Schematic diagram showing the phantom design with labels representing distances of the seeds from the light source. The light is directed toward the seed located 1 cm from the light source (i.e., 2.3 cm from the probe), and it was rotated to visualize the other seeds. (b) Photograph of phantom.

an energy density of 111 mJ/cm^2 at the surface of the quartz tube.

A photoacoustic imaging system consisting of a US scanner (SonixTouch, Ultrasonix, Richmond, BC, Canada), transrectal US probe with dual linear and curvilinear arrays (BPL9-5 and BPC8-4, Ultrasonix), data acquisition unit (SonixDAQ, Ultrasonix), and the 1064-nm Phocus InLine Nd:YAG laser was utilized to acquire photoacoustic data. The laser was coupled to the free end of the side-firing optical fiber. Prebeamformed photoacoustic images were displayed in real time at a rate of 3 to 5 frames per second to assist with seed localization. The software framework for real-time photoacoustic imaging with this system was described in a previous publication,[38] while the commercial SonixTouch US system and software were utilized to acquire linear and curvilinear US images (i.e., images acquired with the linear and curvilinear arrays, respectively). The sampling rate for data acquisition was 40 MHz, and the bandwidths of the linear and curvilinear arrays were 4 to 8 MHz and 5 to 9 MHz, respectively.

2.4 Monte Carlo Simulation

To investigate light propagation beyond the urethral walls in an optically scattering medium, a 3-D Monte Carlo simulation[39] was performed with a 1 cm × 1 cm × 1 cm cubic voxel of prostate tissue and a resolution cell of 50 μm in each dimension. The light source incident on the urethral wall (i.e., centered on one surface of the prostate voxel) was a 1.2 mm × 1.8 mm ellipse with a focus located 2.1 mm from the prostate tissue (i.e., inside the urethra), which corresponds to the geometrical dimensions of the elliptical light cone produced by our fiber prototype. A 0.1-mm air interface separated the light source from the urethra.

The prostate contained three 0.8 mm × 4.5 mm cylindrical targets (i.e., brachytherapy seeds) at radial distances of 5.0, 5.4, and 5.8 mm from the center of the light source incident on the urethra. The circumference of the seeds intersected the x-z plane, and the length of the seeds was coincident with the y-z plane. To demonstrate the expected differences in light distribution with the implantation of additional seeds, a fourth seed was added with its center offset by 0.3 mm from the x = 0 plane at a radial distance of 3 mm from the center of the light source incident on the urethra. The run times for the three- and four-seed simulations were 20 and 8 min, respectively, resulting in a total of ~1.3 × 10^6 photons launched for each simulation.

Optical properties were modeled at a laser wavelength of 1064 nm, using the values for canine prostates[40] and 100% India ink[41] reported in Table 2. Note that the optical absorption of India ink is similar (within an order of magnitude) to that of stainless steel brachytherapy seeds.[11]

Table 2 Optical parameters for three-dimensional Monte Carlo simulation.

	μ_a (cm^{-1})	μ_s (cm^{-1})	g (cm^{-1})
Prostate	0.27	3.06	0.45
India ink	2000	1000	0.9

2.5 Canine Experiments

Two canine prostates were implanted with cylindrical (0.8 mm outer diameter, 4.5 mm long axis), decayed, coated brachytherapy seeds under transrectal US guidance, as approved by the Johns Hopkins Animal Care and Use Committee. The abdomen of each dog was opened to access the prostate and insert the urinary catheter. For the first dog, seeds were implanted transperineally, similar to a human procedure, prior to the abdominal surgery. For the second dog, the seeds were inserted directly into the prostate after the surgery with an orientation similar to a human procedure. This approach enabled precise targeting of difficult-to-image regions of the prostate.[42,43] A 16-Fr (i.e., 5.3 mm outer diameter) silicone urinary catheter (Model 1658-16 Bardex®) was inserted through an incision in the bladder to avoid the curvature of the urethra near the canine's pubic bone, which is more pronounced than that of humans. The side-firing fiber was inserted into the open end of the catheter to image the implanted brachytherapy seeds.

Using the US and photoacoustic imaging systems described in Sec. 2.3, the first prostate was imaged in the native tissue environment, 1 to 2 h after euthanasia. The average energy per pulse was 6.7 mJ, which corresponds to an energy density of 370 mJ/cm^2 at the surface of the quartz tube. The radial distance between the center of the urethra and the three seeds that were imaged was 6 to 9 mm, as measured in the curvilinear US image. The second prostate was imaged *in vivo* with an average energy per pulse of 7.5 mJ, which corresponds to an energy density of 414 mJ/cm^2 at the surface of the quartz tube. The radial distance between the center of the urethra and the seed was 1 cm.

The locations of implanted seeds were confirmed with intraoperative US images and postoperative computed tomography (CT) images. The transrectal US probe was locked in place with a brachytherapy stepper (Nucletron, Veenendaal, The Netherlands) to acquire coregistered US and photoacoustic images.

2.6 Beamforming Photoacoustic Data

A conventional delay-and-sum (DAS) beamformer and a coherence-based short-lag spatial coherence (SLSC) beamformer[28,44] were applied to the zero-mean radiofrequency (RF) photoacoustic signals received by the transducer. Received signal time delays were calculated with 33-element subapertures to limit off-axis acoustic clutter. Hanning apodization was applied to the delayed signals for DAS beamforming with no apodization applied for SLSC images. The parameters for SLSC imaging were adjusted to optimize seed visualization as described in previous publications,[18,28] where M, the short-lag value for integration of coherence functions, was equal to 10 for curvilinear images and 4 for linear images (i.e., 30 and 12% of the active receive aperture, respectively). The correlation kernel length was equivalent to the smallest wavelength within the bandwidth of the linear array (i.e., 0.308 mm). The beamformed photoacoustic data were envelope-detected, normalized to the brightest image pixel, and log compressed. In addition, images acquired with the curvilinear array were scan converted. No aperture growth, RF frame averaging, nor compensation for optical attenuation was implemented for either beamformer.

To assess image quality, the contrast of seed signals in DAS and SLSC photoacoustic images were calculated using the definition, Contrast = $20 \log_{10}(S_i/S_o)$, where S_i and S_o are the means of the envelope-detected RF data within regions of

interest (ROIs) located inside and outside of a brachytherapy seed. Comparative lateral resolutions were measured as the full width at half maximum (FWHM) of line plots passing through the center of seed signals. US and photoacoustic image processing and image analyses were performed with MATLAB® software (The MathWorks, Inc., Natick, Massachusetts), while CT image analyses were performed with ImageJ software.[45]
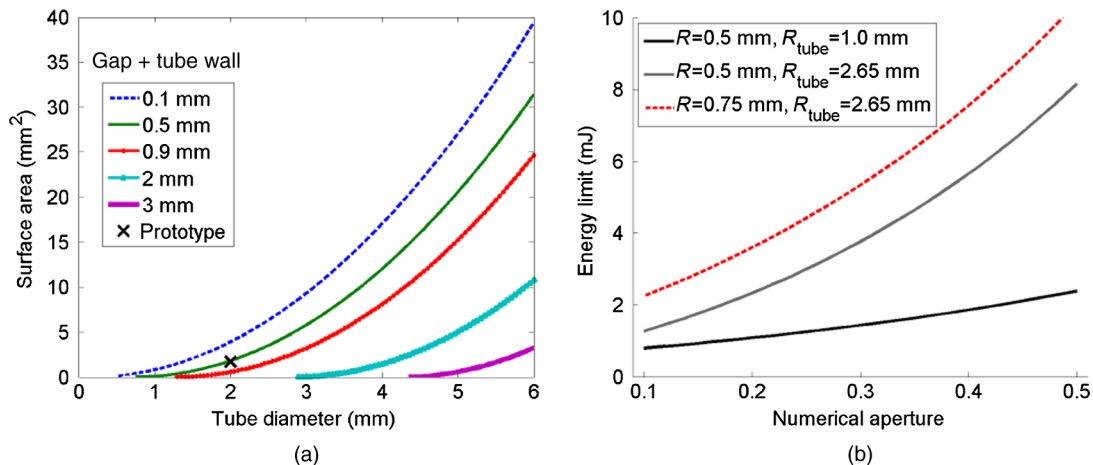
3 Results

3.1 Design Parametrization

Equations (1) and (2) show that the minor and major axes of the elliptical light profile depend on the NA of the fiber, the tube inner and outer diameters, the fiber diameter, and the minimal air gap spacing between the fiber and tube. The latter parameters are related through the expression $R_{tube} - R$, which represents the combined tube thickness and air gap spacing. As illustrated in Fig. 4(a), increasing these parameters increases the surface area.

Figure 4(b) shows the energy limits required to satisfy the 100 mJ/cm^2 safety limit for skin exposure at a wavelength of 1064 nm,[46] as the NA was varied from 0.1 to 0.5. Results are shown for optical fibers with 1 and 1.5 mm core diameters (i.e., $R = 0.5$ and 0.75 mm, respectively), tube diameters of 2.0 and 5.3 mm (i.e., $R_{tube} = 1.0$ and 2.65 mm, respectively), and the remaining parameters listed in Table 1. These calculations indicate that the energy limit increases with larger NAs, fiber diameters, and tube diameters, due to the larger surface area of the laser beam that exits the fiber. This result can be modified for different fiber parameters, using Eq. (5) to determine the energy limits required to remain below any given energy density limit.

Limits to the maximum achievable surface area and energy limit in Figs. 4(a) and 4(b), respectively, include the size of the urethra and the inner diameter of the catheter when present (e.g., 6 and 2 mm, respectively), as well as additional mechanical design constraints (e.g., minimum required bending radius, stresses applied during fiber insertion) and ergonomic considerations (e.g., patient comfortability with large catheters), which are beyond the scope of this paper.
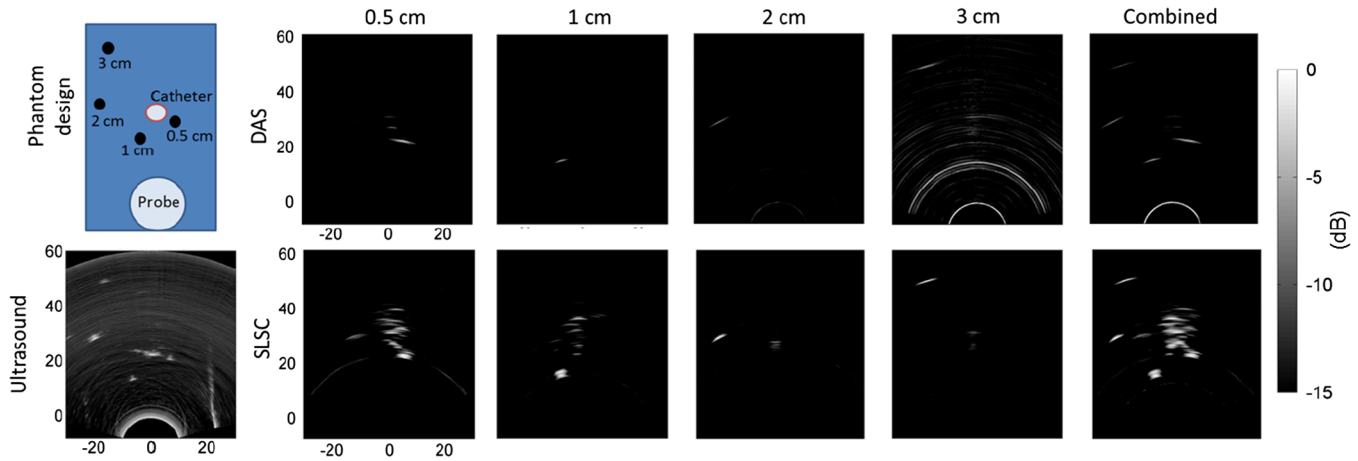
3.2 Beamformer Comparisons

A cross-sectional schematic of the phantom design and curvilinear US and photoacoustic images created with the DAS and SLSC beamformers are shown in Fig. 5. The fiber was rotated to visualize each seed located at distances of 0.5 to 3 cm from the catheter. The mean contrast of DAS images varied from 20 dB for the seed located 0.5 cm from the light source to 9 dB for the seed located 2.8 cm from the light source. Seeds located 2 to 3 cm from the catheter were better visualized with the SLSC beamformer, which provided a 12 to 29 dB mean contrast improvement over the DAS images, as shown in Fig. 6(a).

Eight images of each seed were summed and shown with a 15 dB dynamic range in the last column of Fig. 5. The seeds farthest from the light source are more difficult to locate in the combined DAS image due to the decreasing contrast with distance. However, the combined SLSC image (bottom right) shows a clear map of the location of the four implanted seeds, regardless of distance from the light source, and it closely resembles the US image (bottom left). The SLSC image also amplifies the coherent photoacoustic artifacts associated with the urinary catheter location. One solution to minimize these artifacts is to limit the dynamic range of the SLSC image, which would not affect seed visualization, as the seeds are more coherent than the artifacts. On the other hand, increasing the dynamic range of the combined DAS image would enhance visualization of the farthest seed but increase the background noise in the image.

Examples of line profiles passing through the seeds located at 0.5 and 3 cm from the urinary catheter are displayed prior to scan conversion (i.e., as a function of azimuthal angle) in Fig. 6(b). The line profiles for the seed located at 0.5 cm from the catheter in DAS and SLSC images were taken from the same image depth (i.e., 1.7 cm from the probe) and displayed with the maximum signals aligned. The coherent background signals observed to the left and right of the seed closest to the catheter (located 0.5 cm away) is likely due to clutter, electronic noise, and the off-axis spatial coherence of catheter signals. These line plots demonstrate that the background noise in SLSC images has more variance, which causes the larger

Fig. 4 (a) Elliptical surface area as the tube diameter and $R_{tube} - R$ (i.e., the combined tube wall thickness and air gap between fiber and quartz tube) are varied. The black **x** denotes parameters of the custom-built prototype. (b) Energy limits were calculated for various numerical aperture values given the fiber and tube radii corresponding to the prototype ($R = 0.5$ mm and $R_{tube} = 1.0$ mm, respectively), a tube radius corresponding to the urinary catheter ($R_{tube} = 2.65$ mm), and a larger fiber radius ($R = 0.75$ mm).

Fig. 5 Phantom schematic diagram and curvilinear ultrasound (US) image of the phantom are shown on the left. Delay-and-sum (DAS) (top) and short-lag spatial coherence (SLSC) (bottom) photoacoustic data were created after the fiber was rotated toward each seed. The distances between the light source and seed are indicated in the schematic diagram and above each image. The far right displays results after summing eight DAS (top) and SLSC (bottom) images from each fiber rotation. The scales on the left images have units of millimeter and correspond to all photoacoustic images, which are all shown with 15 dB dynamic range, as indicated by the colorbar on the right.
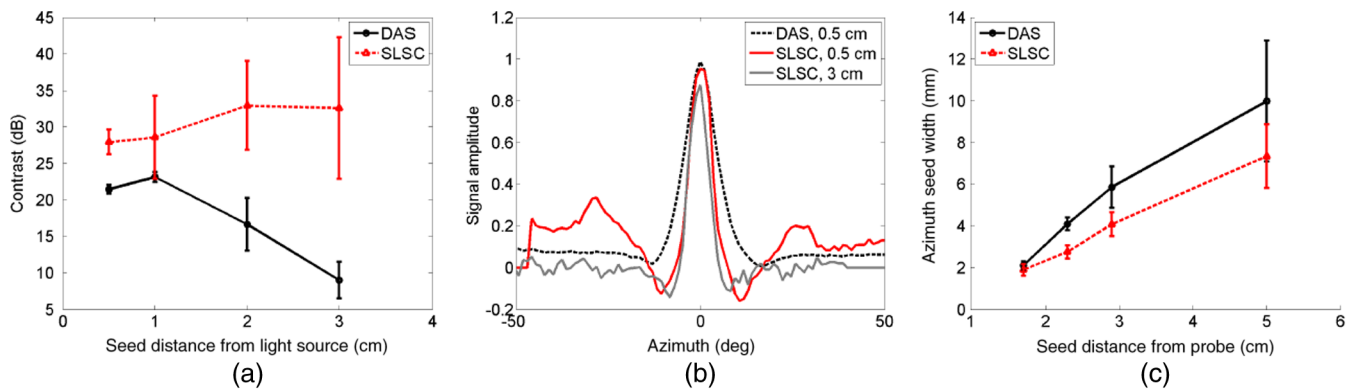
Fig. 6 (a) Contrast, (b) line profiles, with values in the legend representing distances from the light source to the seed, and (c) full width at half maximum (FWHM) measurements from DAS and SLSC photoacoustic images acquired with the curvilinear array.

standard deviations for SLSC contrast measurements. In addition, note that the contrast measurement is dependent on the location of the noise ROI relative to the surrounding clutter.

The line profiles in Fig. 6(b) and similar line profiles for each seed were used to measure the FWHM of the seed signals and obtain comparative estimates of lateral resolution. These measurements were performed on prescanconverted images, converted from degrees to distance, and reported as a function of distance from the probe in Fig. 6(c). Results show the mean measurements from eight images for each seed ± one standard deviation. The actual seed width is 0.8 mm in this dimension, which both beamformers overestimate.

Two of the same seeds visualized with the linear array are shown in Fig. 7(a). The distance between the light source and seeds is indicated in the US image (left) and above each photoacoustic image created with DAS (top) and SLSC (bottom) beamformers. The width of the phantom is 2 cm in the lateral image dimension, and the air tracks created from seed insertion appear to the left of the seeds in the US image. Similar to the curvilinear results, photoacoustic images created

with the SLSC beamformer have 10 to 27 dB higher contrast than images created with the DAS beamformer, particularly when the seeds are located 2 to 3 cm from the light source.

For the seed located 1 cm from the light source, SLSC images have more apparent clutter compared to the DAS image, which is similarly true for the curvilinear image of this seed. In both cases, light was directed toward the probe, causing less sound attenuation by the air inside the catheter. The increased potential for multiple acoustic reflections among the seed, probe, and catheter boundary strongly indicates the source of this additional clutter. Figure 7(b) shows the mean lateral FWHM measurements from eight images for each seed ± one standard deviation. The actual seed length (4.5 mm) is underestimated for the seeds located closer to the probe.

These beamforming results demonstrate that multiple seeds at a range of distances from the light source in curvilinear images can be visualized with similar contrast and no attenuation compensation required for the SLSC beamformer. On the other hand, seeds in linear images affected by multiple clutter sources (e.g., proximity to the light source, acoustic

(a)

(b)
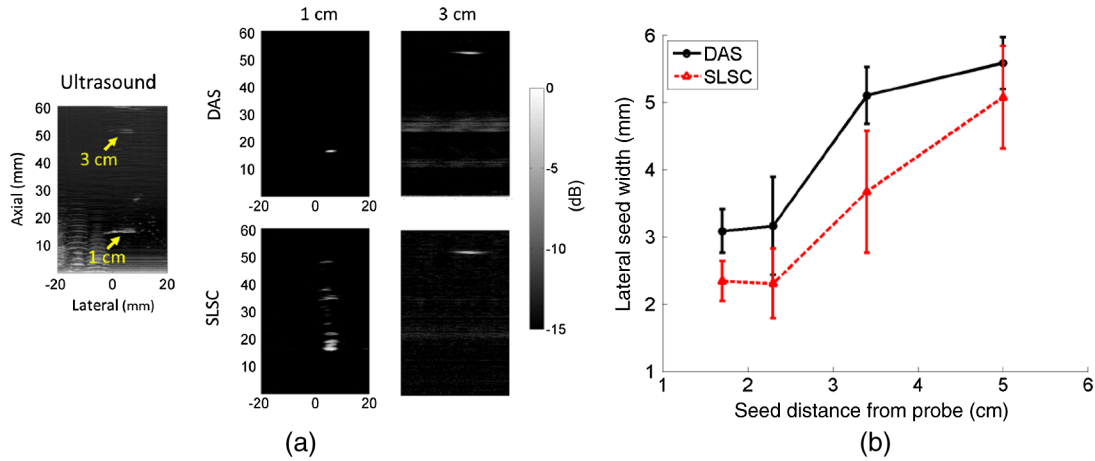
Fig. 7 (a) The linear US image on the left shows seeds in the phantom located at 1 and 3 cm from the catheter. DAS (top) and SLSC (bottom) photoacoustic data were created after the fiber was rotated toward each seed. The distances between the light source and seed are indicated above each image. The scales on the left images have units of millimeter and correspond to all photoacoustic images, which are all shown with 15 dB dynamic range, as indicated by the colorbar on the right. (b) Mean $\pm$ one standard deviation of the lateral FWHM of all seeds in the phantom.

reverberations within the catheter, and acoustic reflections between the catheter and probe) are better visualized with the DAS beamformer, which is less sensitive to low-amplitude, spatially coherent clutter. These observations determined the beamformer choice for displaying the remaining photoacoustic images.

3.3 Light Delivery in Scattering Media

The normalized fluence distribution of light from an elliptical surface area source is shown for three seed-like targets in Fig. 8 (left), representing cross-sectional views that might be obtained with the curvilinear and linear arrays (top and bottom, respectively). As expected, the targets farthest from the light source experience the least fluence, with at most 10 J/cm^2 per J experienced by the closest seed, as depicted in the z-y plane. When a fourth seed was added to the simulation (Fig. 8, right), representing a partially out-of-plane seed for the linear array, light distribution to the original three seeds was reduced by one to two orders of magnitude, which indicates the difficulty with using fixed light attenuation models to improve target visualization with the DAS beamformer. In both simulations, the fluence delivered within a 1 cm radius from a light source was two to four orders of magnitude lower than the maximum fluence observed in the prostate tissue.
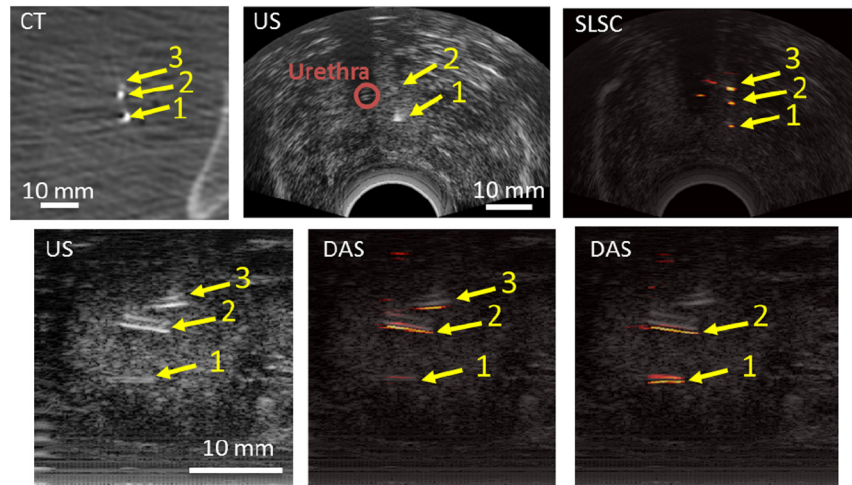
A postoperative CT image of three brachytherapy seeds implanted in one canine prostate with geometry similar to the three-seed simulation is shown in Fig. 9 (top left). Seeds #2 and 3 are separated by <2 mm. A corresponding curvilinear US image is shown in Fig. 9 (top center). The urethra containing the 16-Fr urinary catheter is outlined with a circle. This catheter causes a shadow artifact in the curvilinear US image (i.e., the dark region extending from the urethra). Seeds #1 and 2, located at radial distances of 6 to 9 mm from the center of the urethra, are visible in this US image. A single SLSC photoacoustic image (top right) reveals the three implanted seeds, along with photoacoustic signals that correspond to the catheter location. The seed farthest from the light source (#1) was not visualized in the matching DAS image (not shown).

The three seeds are visualized in the linear US image of the same prostate, as shown in Fig. 9 (bottom left). In this image, seeds #2 and 3 are closely spaced and appear in the same plane, while seed #1 is partially outside of the image plane. When light was directed toward the in-plane seeds (#2 and 3), these seeds were more visible than the out-of-plane seed (#1) with DAS beamforming, as shown in Fig. 9 (bottom middle). When light was directed toward the out-of-plane seed, both this seed and the nearby in-plane seed (seeds #1 and 2, respectively) appeared in the DAS photoacoustic image (Fig. 9, bottom right). These results indicate that the side-firing fiber combined with amplitude-based beamforming can be used to selectively differentiate closely spaced targets.
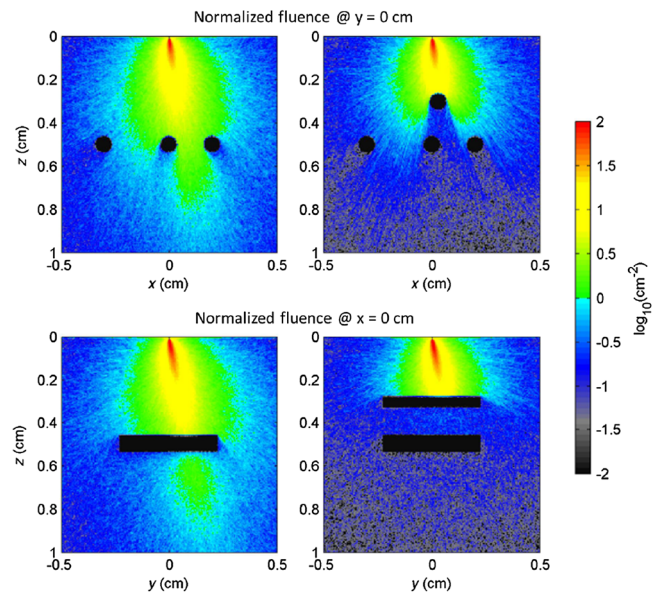
Fig. 8 Cross-sectional views of normalized fluence beyond the urethral wall in prostate tissue containing three (left) and four (right) seed-like targets in log compressed units of cm^{-2} [i.e., $\log_{10}$ (J/cm^2 per J) of energy delivered].

Fig. 9 Postoperative computed tomography (CT) image of three brachytherapy seeds in a canine prostate and corresponding US and photoacoustic SLSC and DAS images of the seeds, acquired after euthanasia. The photoacoustic images were overlaid on the US images and share the same scale indicated in the corresponding curvilinear or linear US image.

The postoperative CT image of a brachytherapy seed implanted in the second canine prostate is shown in Fig. 10 (top left). The catheter in the urethra appears as a faint circle in the CT image, while the seed appears as a bright spot. The seed was implanted in the apex of the prostate, which is known to be difficult to visualize in the sagittal view of transrectal ultrasound images,[42,43] as demonstrated in the US image of Fig. 10, where the arrow points to the seed. The corresponding photoacoustic image, overlaid on the US image, contains the seed as well as signals in the urethra and associated reverberation artifacts. The comet-tail-like reverberation artifacts were less prevalent in matched DAS images (not shown) and not present in SLSC images when the fiber tip was outside of the image plane, as demonstrated in Figs. 5 and 9. Note that these reverberation artifacts (likely caused by the metal tip) have a different characteristic appearance from the catheter-related clutter in Fig. 5. The shadow artifact in the corresponding US image (i.e., the dark region caused by poor acoustic penetration through the catheter) was used to create a mask and set a threshold for signal rejection, resulting in a seed that is clearly differentiated from its surroundings. A similar mask may be used to hide the less prominent photoacoustic signals originating within the catheter (e.g., Fig. 9). The linear US image in Fig. 10 (bottom left) shows a longitudinal view of the same seed, which is better visualized and more easily distinguishable in the corresponding photoacoustic image (Fig. 10, bottom right).

4 Discussion

4.1 Considerations for Transurethral Illumination

To demonstrate the feasibility of transurethral photoacoustic imaging, brachytherapy seeds were visualized in a plastisol phantom and in two canine prostates with 2 mJ and 6 to 8 mJ per pulse, respectively, at distances of 5 to 30 mm and 6 to 9 mm from the light source, respectively. The two canine prostates were imaged in their native tissue environments, in the presence of competing endogenous and *in vivo* chromophores, such as blood, proteins, water, and lipids, indicating that a similar performance can be expected with transurethral photoacoustic imaging of tumors and contrast agents.
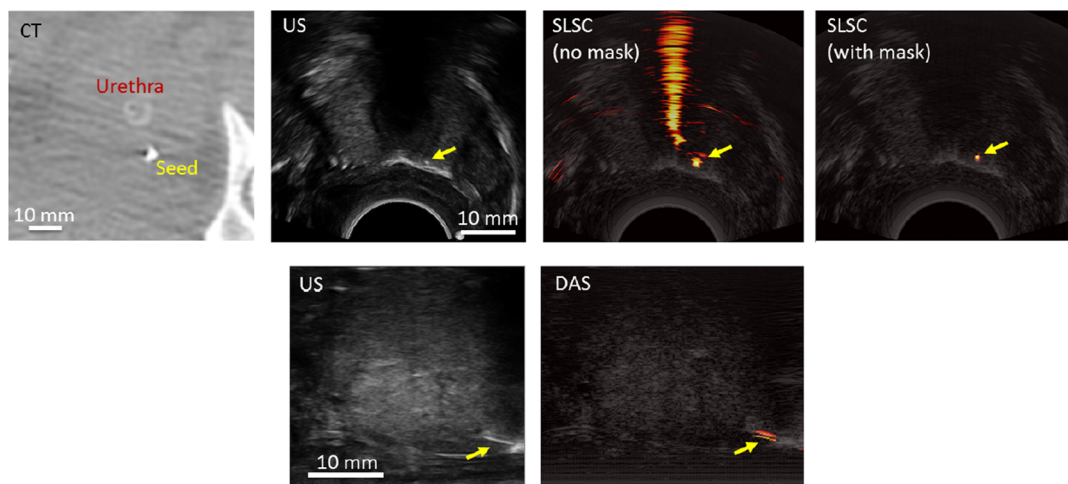
Fig. 10 *In vivo* CT, US, and photoacoustic SLSC and DAS images of a brachytherapy seed in the apex of the prostate. The photoacoustic images were overlaid on the US images and share the same scale indicated in the corresponding curvilinear or linear US image.

Monte Carlo simulations performed by El-Gohary et al.[33] revealed that the optimal optical beam geometry for imaging spherical tumors with a diameter of 2 to 10 mm was a 4 mm × 20 mm rectangle. Figure 4(a) shows that the corresponding surface area (80 mm²) is not practical with the design herein, given the physical constraints of catheter size, urethra diameter, tube wall thickness, fiber size, and a fixed NA of 0.39. In spite of these constraints, sufficient fluence was delivered to smaller targets (0.8 mm × 4.5 mm cylinders), as confirmed with our simulations and canine experiments. If larger surface areas are required, a light delivery mechanism similar to our prototype can be translated or rotated within the urethra and the resulting images may be compounded (as demonstrated in Fig. 5) to fully visualize the larger targets.

Several side-firing fiber prototypes have been designed and built for photoacoustic imaging by manipulating the fiber tip (e.g., relying solely on total internal reflection to direct light through the side of a fiber or adding an external mirror to an end-firing fiber) and fixing the modified fiber relative to a US transducer.[35,47] Our design differs from these approaches by combining the effects of internal and external reflection and separating the light delivery mechanism from the US transducer. Benefits of this novel design include directing light 90 deg to the fiber axis with minimal energy lost to significantly smaller or larger angles, utilizing more than one piezoelectric element to receive photoacoustic signals, and obviating the need to maintain a fixed overlap between light emission and sound reception. This design is challenged by reverberation artifacts caused when the metal tip intersects the image plane, which is potentially useful for identifying the fiber tip inside the urethra. After tip identification, the artifacts could be removed with an image mask as demonstrated in Fig. 10 or mitigated by preventing intersection with the image plane as in Figs. 5 and 9.

The reported energy densities at the tube surface in the canine experiments (Figs. 9 and 10) exceeded the safety limit for skin (i.e., 100 mJ/cm² with a 1064 nm wavelength[46]), but the main safety concern should be the energy density at the first laser-tissue contact interface (i.e., the urethra), which is likely lower than the reported values. Assumptions to achieve more relevant estimates include negligible energy loss between the quartz tube and catheter, negligible spacing between the fiber and catheter (and, therefore, negligible light diffraction in the urine), no deformation of the cylindrical catheter, and similar light refraction in the catheter and quartz tube given the similar refractive indices of their constituents (i.e., silicone and silicon dioxide, respectively[48,49]). Based on these assumptions and Eq. (4), the energy density incident on the urethra with a 0.49 NA, 1 mm core diameter fiber, and 5.3 mm tube diameter (i.e., the outer diameter of the catheter) is 88 to 99 mJ/cm², which is within the limit for skin exposure. In addition, Fig. 4(b) shows that the energies used in the canine experiments would have been <75% of the safety limit if the fiber diameter were 1.5 mm instead of 1 mm. Moreover, the prostate and urethra could potentially withstand higher energy densities than the existing limit for skin.[11] The derived equations enable nonempirical surface area estimates that can be used to further explore safety limits and photon transport with Monte Carlo simulations.

4.2 *Importance of the Image Reconstruction Method*

Consistent with previous results achieved with interstitial transperineal light delivery,[17,28] the contrast of DAS images generally decreased with increasing distance from the light source, a direct effect of the decreasing incident fluence, which produces lower photoacoustic signal amplitudes. Rotating the direction of the light source and combining the resulting SLSC photoacoustic images acquired with the curvilinear array is an alternative to depth-dependent optical attenuation compensation, which requires an optical distribution model that is subject to change with the implantation of additional brachytherapy seeds (e.g., Fig. 8). This model is difficult to develop when the target locations are unknown (e.g., tumors) or dynamic (e.g., brachytherapy seed implantation).

Thus, coherence-based beamforming is an essential component of the proposed photoacoustic system because it allows target locations to be directly compared with postoperative CT and curvilinear US B-mode images, without application of a light distribution model. Although more advanced summation approaches may be applied to improve the combined DAS images, they are not required for SLSC imaging as demonstrated in Fig. 5. Once targets have been located with the SLSC beamformer, the DAS beamformer would be more advantageous for providing isolation and discrimination of in-plane or out-of-plane targets relative to the US probe and near or far targets relative to the light source, as demonstrated in Fig. 9.

4.3 *Optical and Acoustic Resolution Limits*

Comparative resolution was assessed with FWHM measurements, revealing minimal (0 to 3 mm) differences in target size with the DAS and SLSC beamformers. In curvilinear images, the seed diameter increased with distance from the probe [Fig. 6(c)] likely because of the increase in lateral beam width. The measured diameter was generally larger than the actual diameter because of the finite acoustic aperture size and the optical diffraction limited resolution. In linear images, the seed appeared longer with distance from the probe [Fig. 7(b)] likely because of the absence of aperture growth in the receive beamformer or the increasing area of light illumination incident on the seed as distance increased. This relationship between the optical illumination area and the displayed seed length, particularly within 0.5 to 1 cm from the urethra [Fig. 7(b)], is mitigated with optical scattering in tissue, as shown in the simulation (Fig. 8) and canine images (Figs. 9 and 10).

5 Conclusion

This is the first study to implement transurethral light delivery for photoacoustic imaging of prostates, demonstrating feasibility in phantoms, *ex vivo*, and *in vivo*. A method to determine the surface area of light exiting a side-firing optical fiber and surrounding quartz tube was derived and utilized to estimate energy densities and simulate scattering in prostate tissue. The limits for our design parameters are related to optical and physical constraints (e.g., NA, fiber and tube diameters, urethra size, catheter size). Reasonable parameters within these constraints were utilized to build a side-firing fiber that enabled preferential illumination of targets. Equally visible images of each target were obtained with the SLSC beamformer with no optical or acoustic attenuation compensation required, despite the varying distances from the light source, while the DAS beamformer offered better discrimination of closely spaced, in-plane, out-of-plane, near, or far seeds. In addition, 3-D Monte Carlo simulations demonstrated that the light distribution is highly dependent on target location; hence, applying optical attenuation models may not

always be feasible for enhancing amplitude-based beamformers. Similar results are expected for visualization of prostate cancers and exogenous contrast agents delivered to the prostate. The proposed light delivery and beamforming methods promise to improve key prostate cancer detection and treatment strategies.

Acknowledgments

References

1. S. Zackrisson, S. M. W. Y. van de Ven, and S. S. Gambhir, "Light in and sound out: emerging translational strategies for photoacoustic imaging," *Cancer Res.* **74**(4), 979–1004 (2014).
2. M. Xu and L. V. Wang, "Photoacoustic imaging in biomedicine," *Rev. Sci. Instrum.* **77**(4), 041101 (2006).
3. S. Rosenzweig et al., "Advanced ultrasound: prostate elastography and photoacoustic imaging," in *Image Guided Prostate Cancer Treatments*, pp. 31–45, Springer (2014).
4. P. Tenke et al., "Prostate cancer screening," in *Prostate Cancer*, pp. 65–81, Springer (2007).
5. S. E. M. Langley and R. Laing, "Prostate brachytherapy has come of age: a review of the technique and results," *BJU Int.* **89**(3), 241–249 (2002).
6. B. H. Han et al., "Prostate brachytherapy seed identification on post-implant trus images," *Med. Phys.* **30**, 898 (2003).
7. C. F. Serago et al., "Initial experience with ultrasound localization for positioning prostate cancer patients for external beam radiotherapy," *Int. J. Radiat. Oncol. Biol. Phys.* **53**(5), 1130–1138 (2002).
8. D. A. Kapoor et al., "Value of transrectal ultrasound in identifying local disease after radical prostatectomy," *Urology* **41**(6), 594–597 (1993).
9. H. B. Carter et al., "Evaluation of transrectal ultrasound in the early detection of prostate cancer," *J. Urol.* **142**(4), 1008–1010 (1989).
10. B. Nicholson, G. Schaefer, and D. Theodorescu, "Angiogenesis in prostate cancer: biology and therapeutic opportunities," *Cancer Metastasis Rev.* **20**(3–4), 297–319 (2001).
11. J. L. Su et al., "Photoacoustic imaging of prostate brachytherapy seeds," *Biomed. Opt. Express* **2**(8), 2243–2254 (2011).
12. J. Su et al., "Photoacoustic imaging of clinical metal needles in tissue," *J. Biomed. Opt.* **15**(2), 021309 (2010).
13. F. Rabbani et al., "Incidence and clinical significance of false-negative sextant prostate biopsies," *J. Urol.* **159**(4), 1247 (1998).
14. L. A. Eskew, R. L. Bare, and D. L. McCullough, "Systematic 5 region prostate biopsy is superior to sextant method for diagnosing carcinoma of the prostate," *J. Urol.* **157**(1), 199–203 (1997).
15. N. Kuo et al., "Real-time photoacoustic imaging of prostate brachytherapy seeds using a clinical ultrasound system," *J. Biomed. Opt.* **17**(6), 066005 (2012).
16. T. Harrison and R. J. Zemp, "Coregistered photoacoustic-ultrasound imaging applied to brachytherapy," *J. Biomed. Opt.* **16**(8), 080502 (2011).
17. M. A. Lediju Bell et al., "*In vivo* visualization of prostate brachytherapy seeds with photoacoustic imaging," *J. Biomed. Opt.* **19**(12), 126011 (2014).
18. E. M. Boctor et al., "Prostate brachytherapy seed localization using combined photoacoustic and ultrasound imaging," presented at *Ultrasonic Imaging, Tomography and Therapy Medical Imaging*, 14 February 2010, 7629, SPIE, San Diego, California.
19. J. E. Dawson et al., "Dose effects of seeds placement deviations from pre-planned positions in ultrasound guided prostate implants," *Radiother. Oncol.* **32**(3), 268–270 (1994).
20. P. L. Roberson et al., "Source placement error for permanent implant of the prostate," *Med. Phys.* **24**(2), 251–257 (1997).
21. J. F. Anderson et al., "Urinary side effects and complications after permanent prostate brachytherapy: the MD Anderson Cancer Center experience," *Urology* **74**(3), 601–605 (2009).
22. D. Bottomley et al., "Side effects of permanent i125 prostate seed implants in 667 patients treated in Leeds," *Radiother. Oncol.* **82**(1), 46–49 (2007).
23. N. N. Stone and R. G. Stock, "Complications following permanent prostate brachytherapy," *Eur. Urol.* **41**(4), 427–433 (2002).
24. K. Wilson, K. Homan, and S. Emelianov, "Biomedical photoacoustics beyond thermal expansion using triggered nanodroplet vaporization for contrast-enhanced imaging," *Nat. Commun.* **3**, 618 (2012).
25. A. Agarwal et al., "Targeted gold nanorod contrast agent for prostate cancer detection by photoacoustic imaging," *J. Appl. Phys.* **102**(6), 064701 (2007).
26. G. P. Luke, D. Yeager, and S. Y. Emelianov, "Biomedical applications of photoacoustic imaging with exogenous contrast agents," *Ann. Biomed. Eng.* **40**(2), 422–437 (2012).
27. R. E. Kumon, C. X. Deng, and X. Wang, "Frequency-domain analysis of photoacoustic imaging data from prostate adenocarcinoma tumors in a murine model," *Ultrasound Med. Biol.* **37**(5), 834–839 (2011).
28. M. A. Lediju Bell et al., "Short-lag spatial coherence beamforming of photoacoustic images for enhanced visualization of prostate brachytherapy seeds," *Biomed. Opt. Express* **4**(10), 1964–1977 (2013).
29. K. Valluru et al., "Probe design for photoacoustic imaging of prostate," in *IEEE Int. Conf. on Imaging Systems and Techniques*, Thessaloniki, 121–124, IEEE (2010).
30. M. A. Yaseen et al., "Hybrid optoacoustic and ultrasonic imaging system for detection of prostate malignancies," *Proc. SPIE* **6856**, 68560T (2008).
31. M. A. Yaseen et al., "Optoacoustic imaging of the prostate: development toward image-guided biopsy," *J. Biomed. Opt.* **15**(2), 021310 (2010).
32. M. A. Lediju Bell et al., "Photoacoustic imaging of prostate brachytherapy seeds with transurethral light delivery," *Proc. SPIE* **8943**, 89430N (2014).
33. S. H. El-Gohary et al., "Design study on photoacoustic probe to detect prostate cancer using 3D Monte Carlo simulation and finite element method," *Biomed. Eng. Lett.* **4**(3), 250–257 (2014).
34. W. Xie et al., "Photoacoustic imaging of prostate cancer using cylinder diffuse radiation," *Proc. SPIE* **8553**, 85532V (2012).
35. A. B. Karpiouk, B. Wang, and S. Y. Emelianov, "Development of a catheter for combined intravascular ultrasound and photoacoustic imaging," *Rev. Sci. Instrum.* **81**(1), 014901 (2010).
36. L. Pan et al., "Improving photoacoustic imaging contrast of brachytherapy seeds," *Proc. SPIE* **8581**, 85814B (2013).
37. H. O. Badwan et al., "AnchorSeed for the reduction of source movement in prostate brachytherapy with the Mick applicator implant technique," *Brachytherapy* **9**(1), 23–26 (2010).
38. H. J. Kang et al., "Software framework for spatially tracked pre-beamformed RF data with a freehand clinical ultrasound transducer," *Proc. SPIE* **9040**, 90401W (2014).
39. S. L. Jacques, "Coupling 3D Monte Carlo light transport in optically heterogeneous tissues to photoacoustic signal generation," *Photoacoustics* **4**(2), 137–142 (2014).
40. W. H. Nau, R. J. Roselli, and D. F. Milam, "Measurement of thermal effects on the optical properties of prostate tissue at wavelengths of 1,064 and 633 nm," *Lasers Surg. Med.* **24**(1), 38–47 (1999).
41. A. D. Krainov et al., "Optical properties of mouse biotissues and their optical phantoms," *Opt. Spectrosc.* **115**(2), 193–200 (2013).
42. C. Reynier et al., "MRI/TRUS data fusion for prostate brachytherapy. Preliminary results," *Med. Phys.* **31**(6), 1568–1575 (2004).
43. J. Xue et al., "Localization of linked ^{125}I seeds in postimplant TRUS images for prostate brachytherapy dosimetry," *Int. J. Radiat. Oncol. Biol. Phys.* **62**(3), 912–919 (2005).
44. M. A. Lediju et al., "Short-lag spatial coherence of backscattered echoes: imaging characteristics," *IEEE Trans. Ultrason. Ferroelectr. Freq. Control* **58**(7), 1377–1388 (2011).
45. C. A. Schneider et al., "NIH image to ImageJ: 25 years of image analysis," *Nat. Methods* **9**(7), 671–675 (2012).
46. American National Standards Institute, *Z136. 1. American National Standard for the Safe Use of Lasers* (2007).

47. K. Jansen et al., "Intravascular photoacoustic imaging of human coronary atherosclerosis," *Proc. SPIE* **7899**, 789904 (2011).
48. A. Zajac, E. Hecht, and E. Cummings, *Optics*, 4th ed., Pearson Higher Education (2003).
49. M. Millodot, *Dictionary of Optometry and Visual Science*, Butterworth-Heinemann (2004).

Muyinatu A. Lediju Bell is a postdoctoral fellow at Johns Hopkins University. She completed her PhD in biomedical engineering at Duke University in 2012 and earned her BS degree in mechanical engineering from the Massachusetts Institute of Technology in 2006. Her research interests include image quality improvements in ultrasound and photoacoustic imaging, acoustic wave propagation theories, and clinical translation of novel medical imaging technologies that improve the standard of cancer patient care.

Xiaoyu Guo received his BSc in physics in 2006 from Nanjing University, China. He completed his MS in physics in Rensselaer Polytechnic Institute, Troy, New York, in 2009. Currently, he is a research assistant working with Dr. Etienne-Cummings and Dr. Boctor, and pursuing his PhD in electrical engineering at Johns Hopkins University. His research projects focus on developing novel ultrasound imaging and tracking systems.

Danny Y. Song serves as the clinical director and director of brachytherapy in the Department of Radiation Oncology and Molecular Radiation Sciences at the Johns Hopkins University School of Medicine. His research focus is on technological innovations and image guidance for improving the practice of prostate radiotherapy, as well as clinical research in radiotherapy for prostate cancer and other genitourinary malignancies.

Emad M. Boctor is an assistant professor in the Departments of Radiology and Computer Science at Johns Hopkins University. His interests encompass medical imaging, ultrasound instrumentation, elasticity/thermal/photoacoustic imaging, image-guided intervention, and robotics.